SANDIA REPORT
SAND2022-5405
Printed April 26, 2022

Sandia National Laboratories

Modeling the Vertical Response of an Aeroseismometer Balloon System

Jerry Rouse, Danny Bowman, Alexandra M. Sinclair, Elizabeth A. Silber

Prepared by
Sandia National Laboratories
Albuquerque, New Mexico 87185
Livermore, California 94550

Issued by Sandia National Laboratories, operated for the United States Department of Energy by National Technology & Engineering Solutions of Sandia, LLC.

Available to DOE and DOE contractors from

U.S. Department of Energy
Office of Scientific and Technical Information
P.O. Box 62
Oak Ridge, TN 37831

Telephone: (865) 576-8401
Facsimile: (865) 576-5728
E-Mail: reports@osti.gov
Online ordering: http://www.osti.gov/scitech

Available to the public from

U.S. Department of Commerce
National Technical Information Service
5301 Shawnee Road
Alexandria, VA 22312

Telephone: (800) 553-6847
Facsimile: (703) 605-6900
E-Mail: orders@ntis.gov
Online order: https://classic.ntis.gov/help/order-methods

ABSTRACT

Aeroseismometery is a novel, cutting edge capability that involves balloon based systems for detecting and geolocating sources of infrasound. The incident infrasound from a range of sources such as volcanos, earthquakes, explosions, supersonic aircraft impinges upon the balloon system causing it to respond dynamically. The dynamic response is post-processed to locate the infrasound source. This report documents the derivation of an analytical model that predicts the balloon dynamics. Governing equations for the system are derived as well as a transfer function relating the infrasound signal to the net force on the balloon components. Experimental measurements of the infrasound signals are convolved with the transfer function and the governing equations numerically time integrated to obtain predictions of the displacement, velocity and acceleration of the balloon system. The predictions are compared to the experimental measurements with good agreement observed. The derivation focuses only on the vertical dynamics of the balloon system. Future work will develop governing equations for the swinging response of the balloon to the incident infrasound.

This page left blank.

CONTENTS

LIST OF FIGURES

LIST OF TABLES

1. INTRODUCTION

Infrasonic waves are generated by natural events such as volcanic eruptions, earthquakes and bolides (meteors exploding in the atmosphere), as well as anthropogenic events such as explosions and supersonic vehicles. The infrasound signals (frequencies less than 20 Hz) propagate in the atmosphere up to tens of thousands of kilometers.

A balloon-based system, termed aeroseismometer, is being developed which uses the dynamic response of the balloon system to detect and geolocate sources of infrasound. The system consists of a high altitude balloon, a gondola and an instrumentation package tethered below the gondola. Within the instrumentation package is a magnetometer, a microbarometer (microphone) and an inertial measurement unit (IMU) containing a triaxial accelerometer. The global location of the balloon is obtained from a synthesis of data from the IMU, magnetometer and a global navigation satellite. The microbarometer and accelerometer measurements recorded during the balloon response to an incident infrasound signal are used to geolocate the source.

Recently, a methodology based upon principal component analysis has been developed to post-process the accelerometer data and determine the direction of arrival of the infrasound signal. Using multiple balloons or a single floating balloon and a repeating stationary infrasound source, the geolocation can be triangulated.

An understanding of the physics and dynamics of how the aeroseismometer system is excited and responds to the infrasound is necessary in the development of the capability. This report documents a theoretical analysis of the balloon system, developing a physics-based method to predict the response of the system for a given microbarometer measurement. Predictions of the acceleration response are compared to experimental data. To date only the vertical dynamics of the system has been modeled. It is hypothesized the system experiences pendulum-like swinging motion in response to the infrasound. The swinging produces horizontal accelerations which are used to determine the azimthual direction of arrival. Future work will model the hypothesized pendulum-like swinging motion of the balloon system.

2. BALLOON SYSTEM AND FLIGHT

On July 10, 2020 a ballon system composed of a Raven Aerostar helium filled superpressure balloon, gondola and a styrofoam instrumentation box tethered 30 m below the gondola lifted off from Lemitar, New Mexico at 8:40 local time (14:40 UTC). The styrofoam box contained a Paroscientific Digiquarts infrasound recorder (microbarometer) and an InertialSense IMU having a triaxial accelerometer. A photograph of the system moments after launch is shown in Fig. 2-1.

The properties of the balloon system are listed in Table 2-1. The height and diameter of the inflated balloon envelope were supplied by Raven Aerostar. The density, thickness and Young's modulus of the polyethylene film used for the envelope membrane are taken from standard literature. The diameter and Young's modulus for the 550 lb Paracord tether was located online. The length of the Paracord, dimensions and mass of the gondola and styrofoam box were known.

Height of inflated envelope, [m]	h_e	10.0767
Diameter of inflated envelope, [m]	d_e	10.7137
Density of polyethylene membrane, [kg/m^3]	ρ_{mem}	960
Thickness of polyethylene membrane, [m]	t_{mem}	20×10^{-6}
Young's modulus of polyethylene, [Pa]	E_{poly}	1.1×10^{9}
Length of Paracord, [m]	L_p	30
Young's modulus of Paracord, [Pa]	E_{para}	1.95×10^{9}
Diameter of Paracord, [m]	d_p	3.96875×10^{-3}
Distance from CG of balloon to CG of gondola, [m]	L_{bg}	4.5
Dimensions of gondola, [m]	$w_g \times d_g \times h_g$	$0.3302 \times 0.3302 \times 0.6858$
Mass of gondola, [kg]	m_g	36.2874
Dimensions of styrofoam box, [m]	$w_s \times d_s \times h_s$	$0.2794 \times 0.2286 \times 0.3048$
Mass of styrofoam box, [kg]	m_s	1.49685
Acceleration of gravity, [m/s^2]	g	9.80665

Table 2-1. Balloon system properties.

As the balloon floated west toward Arizona three sets of two 1 ton TNT equivalent bottom-lit surface chemical explosions were detonated at the Energetic Materials Research and Testing Center (EMRTC) in Socorro, New Mexico. The detonation time and the corresponding altitude of the balloon for each explosion are listed in Table 2-2. The balloon altitude varied only 73.7 m at the time of detonation over the four hour window. It is unlikely the balloon experienced significant variation of atmospheric properties and therefore the same properties are used for all six detonations. A plot of the balloon altitude during the entire four hour window is shown in

Figure 2-1. Balloon system as flown on July 10, 2020, moments after launch. The gondola and tethered styrofoam box are visible.

Fig. 2-2 with the time of the detonations indicated by vertical blue lines. The two detonations for each of the three sets were only 30 seconds apart, making the two vertical lines for each set difficult to distinguish in the the figure.

Shot	Detonation Time [h:m:s]	Balloon Altitude [m]
1-A	9:39:59.84 MDT (15:39:59.84 UTC)	20486.958
1-B	9:40:29.98 MDT (15:40:29.98 UTC)	20482.592
2-A	10:40:00.00 MDT (16:40:00.00 UTC)	20451.235
2-B	10:40:30.00 MDT (16:40:30.00 UTC)	20451.923
3-A	13:29:59.94 MDT (19:29:59.94 UTC)	20413.389
3-B	13:30:29.86 MDT (19:30:29.86 UTC)	20413.261

Table 2-2. Source detonation times on July, 10, 2020 at EMRTC in Socorro, New Mexico.

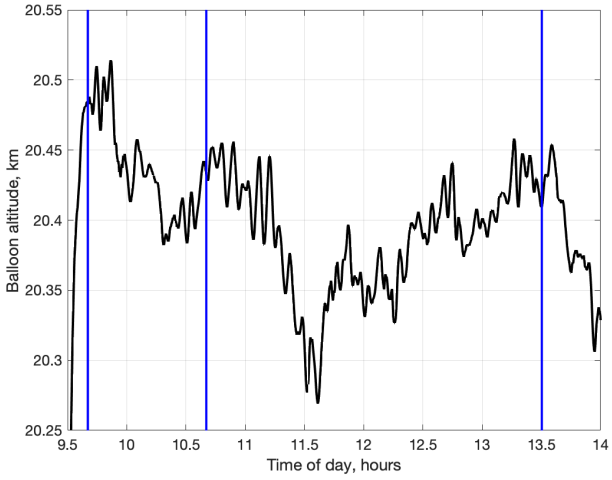

Figure 2-2. Balloon altitude variation during the time window of the EMRTC detonations. The vertical lines indicate the time of the six detonations listed in Table 2-2.

3. MODELING THE BALLOON SYSTEM DYNAMIC RESPONSE

The dynamic response of the balloon system to an incident infrasound signal will now be developed. The following assumptions are made

- For determination of the resulting force from the infrasound, the balloon, gondola and styrofoam box are modeled as spheres
- The mass of the Paracord can be neglected
- The balloon system is in static equilibrium at the float altitude

As a first step, only the vertical motion of the system is considered in this report. It is hypothesized the balloon system actually swings like a pendulum in response to the infrasound. A model of the swing is under development, but due to the complexity of that analysis, the vertical motion was performed first. Also, since not all aspects of the balloon system are known, especially damping, the vertical model can be used to calibrate unknown quantities.

The development shall proceed in the following steps. First, the governing equation for the at-float condition of the balloon system will be derived. The unknown mass of the helium in the balloon envelope will be determined based upon the known properties of the system. The buoyancy stiffness due to the local vertical variation in atmospheric density will also be derived.

In the next step the governing equations for the vertical motion of the balloon system will be developed. Added mass due to the motion of the balloon, gondola and styrofoam box will be included as well as viscous drag due to vertical oscillation of these components. The resonances and mode shapes of the balloon system will be obtained from the system of governing equations. The mode shapes provide insight into the behavior of the system and help to calibrate the viscous damping.

The third step develops a relation between the amplitude of the incident infrasound signal and the net force applied to the balloon, gondola and styrofoam box. Each of these components will be represented as appropriately sized rigid spheres, allowing for an analytical derivation. A frequency domain transfer function will be constructed relating the infrasound to the net force.

In the final step the vertical response of the balloon system to the infrasound signal measured by the microbarometer will be predicted. The governing equations are expressed as a system of 1^{st} order differential equations and numerically time-integrated using the Runge-Kutta numerical method. The predicted acceleration of the styrofoam box is then compared to the experimental data. The unknown damping coefficients for the balloon-to-gondola connection and the Paracord are determined by a frequency domain comparison of the prediction to experiment.

3.1. At-Float Conditions

In the following a series of equations are developed to determine necessary unknown quantities for the analysis. The numerical values computed from these equations are listed in a table at the end of this section.

and V(z) is the volume of the air displaced by the balloon

Let the balloon system at altitude z [m] be represented by a point mass as shown in Fig. 3-1. A buoyancy force $F_b(z)$ [N], equal to the weight of the volume of air $V(z)$ [m^3] displaced by the balloon envelope, offsets the weight W [N] of the system. When $F_b(z) > W$ the balloon ascends into the atmosphere. The acceleration of gravity g varies with altitude, though for the altitudes of interest the sea-level value is sufficient.

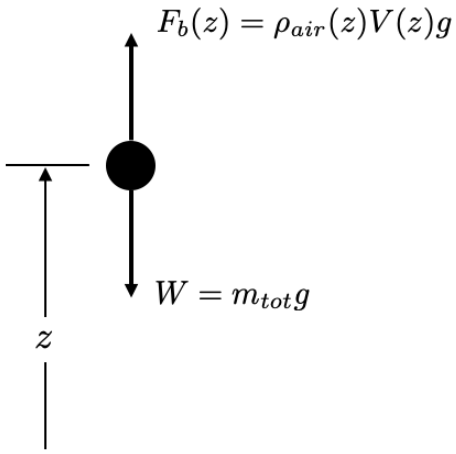

Figure 3-1. Entire balloon system represented as a point mass.

The equation for vertical motion of the balloon system at altitude z is

$$(m_{ba} + m_{tot})\ddot{z}(t) = g\left(\rho_{air}(z)V(z) - m_{tot}\right) \tag{3.1}$$

where $m_{tot} = m_{He} + m_{mem} + m_g + m_s$, [kg] is the sum of the mass of the helium, balloon envelope, gondola, and styrofoam box, ρ_{air} [kg/m^3] is the density of the air, V [m^3] the volume of air displaced by the balloon, and m_{ba} the added mass experienced by the balloon envelope. The balloon floats at altitude z_f when the mass of air displaced by the balloon is equal to the total mass of the system (i.e. the net force is equal to zero):

$$\rho_{air}(z_f)V(z_f) = m_{He} + m_{mem} + m_g + m_s. \tag{3.2}$$

The mass of helium is unknown but can be determined as follows. The mass of the polyethylene balloon envelope membrane $m_{mem} = \rho_{mem}(V(z_f) - V_{int}(z_f))$ where V_{int} is the internal volume of

the balloon. Substituting this expression into Eq. (3.2) and solving for the mass of helium m_{He} gives

$$m_{He} = \left[\rho_{air}(z_f) - \rho_{mem}\right] V(z_f) + \rho_{mem} V_{int}(z_f) - (m_g + m_s). \tag{3.3}$$

Approximating the balloon shape at float as an ellipsoid, the volume of air displaced by the balloon is given by

$$V = \frac{\pi d_e^2 h_e}{6}, \tag{3.4}$$

and for an envelope membrane thickness t_{mem} the volume of helium inside the balloon is

$$V_{int} = \frac{\pi (d_e - 2t_{mem})^2 (h_e - 2t_{mem})}{6}. \tag{3.5}$$

Substituting these expressions into Eq. (3.3) gives an expression for the mass of helium in the balloon envelope:

$$m_{He} = \left[\rho_{air}(z_f) - \rho_{mem}\right] \frac{\pi d_e^2 h_e}{6} + \rho_{mem} \frac{\pi (d_e - 2t_{mem})^2 (h_e - 2t_{mem})}{6} - (m_g + m_s). \tag{3.6}$$

Assuming the helium is uniformly distributed in the envelope, the helium density at float is given by

$$\rho_{He}(z_f) = \frac{m_{He}}{V_{int}} \tag{3.7}$$

Finally, assuming the helium is in thermodynamic equilibrium with the air outside the balloon, the pressure inside the balloon envelope can be obtained from the ideal gas law

$$p_{He}(z_f) = \rho_{He}(z_f) R T_{air}(z_f), \tag{3.8}$$

where $R_{He} = 2076.9$ m^2/(s^2·K) is the gas constant for helium, T_{air} [K] the atmospheric temperature and p [Pa] the atmospheric pressure.

Once the balloon is floating at altitude z_f the equation of motion (3.1) can be expressed in terms of the variation $\bar{z} = z - z_f$ about altitude z_f. The local vertical variation in atmospheric density ρ_{air} can be approximated by a first-order Taylor series

$$\rho_{air}(z) = \rho_{air}(z_f) + \rho'_{air}(z)\big|_{z=z_f} (z - z_f) \tag{3.9}$$

Using the atmospheric variation of density from a standard atmosphere model or weather data, the density at locations Δz above and below the float altitude, $\rho_{air}(z_f + \Delta z)$ and $\rho_{air}(z_f - \Delta z)$, can be used to compute the gradient $M_\rho := \rho'_{air}(z)\big|_{z=z_f}$

$$M_\rho = \frac{\rho_{air}(z_f + \Delta z) - \rho_{air}(z_f - \Delta z)}{2\Delta z}. \tag{3.10}$$

Since the density is smoothly varying at the altitudes of interest $\Delta z \approx 10$ to 20 m.

Substituting $z = z_f + \bar{z}$ and the Taylor series in Eq. (3.9) into Eq. (3.1), the equation of motion can be expressed in terms of $\bar{z}$:

$$(m_{ba} + m_{tot})\ddot{\bar{z}} - g M_\rho V \bar{z} = g\left(\rho_{air} V - m_{tot}\right), \tag{3.11}$$

where ρ_{air} is the value of the atmospheric density at z_f. It has been assumed the perturbation in balloon volume about the float altitude can be neglected.

An uncompressed mass of air around the balloon is accelerated by the motion of the balloon (see Sec. 9-21. of [7]) thereby increasing the apparent mass of the balloon. This additional mass m_{ba} is termed added or hydrodynamic mass and for a sphere the expression for it is well known:

$$m_{ba} = \rho_{air}\frac{2}{3}\pi r_b^3 = \frac{\rho_{air}V}{2}. \tag{3.12}$$

The governing equation for the free vertical motion of the balloon system about the float condition is then

$$\left(\frac{\rho_{air}V}{2} + m_{tot}\right)\ddot{\bar{z}} - gM_\rho V\bar{z} = 0. \tag{3.13}$$

From this equation an expression for the undamped bobbing frequency about the float altitude can be obtained:

$$f_{bob} = \frac{1}{2\pi}\sqrt{\frac{-gM_\rho V}{\frac{\rho_{air}V}{2} + m_{He} + m_{mem} + m_g + m_s}}. \tag{3.14}$$

This expression is similar to that developed by Anderson [2] for a zero-pressure balloon, however here the perturbation of the balloon volume with altitude has not been included.

The acoustic impedance $\rho_{He}a_{He}$ of the helium inside the balloon envelope is of importance. The helium density is given by Eq. (3.7). The speed of sound in the helium is obtained from the ideal gas law and adiabatic compression

$$a_{He} = \sqrt{\gamma_{He}R_{He}T} \tag{3.15}$$

where $\gamma_{He} = 1.667$ is the ratio of specific heats for helium, and temperature T is measured in Kelvin. Assuming the helium is in thermodynamic equilibrium with the air outside the balloon $T = T_{air}$.

Given the balloon system properties listed in Table 2-1, the float altitude $z_f = 20486.96$ m of the ballon at the time of arrival of the first detonation, and the atmospheric variation of density, pressure and temperature from the NCAP G2S Archive (http://g2s.ncpa.olemiss.edu) for the day of the balloon flight, the above equations are used to determine the properties of the balloon system at float. These properties are presented in Table 3-1. Note the slope of the atmospheric density M_ρ is negative due to the decrease in density with altitude and the predicted bobbing frequency f_{bob} is slightly less than the value predicted in [2].

3.2. Governing Equations for Vertical Motion

The governing equations for the vertical motion of the balloon system at the float altitude will now be derived. The balloon, gondola and styrofoam box are treated as point masses connected by springs and dampers. Additional damping due to the viscosity of the air is also included. The system is assumed to be at static equilibrium at the float altitude z (the over-bar has been removed). The balloon system and the equivalent spring-mass-damper model is shown in

Mass of helium in envelope, [kg]	m_{He}	9.589150
Density of helium in envelope, [kg/m^3]	ρ_{He}	1.583391e-02
Speed of sound in the helium, [m/s]	a_{He}	855.9669
Helium pressure, [Pa]	p_{He}	6959.314
Volume of balloon envelope, [m^3]	V	605.6156
Volume of balloon interior, [m^3]	V_{int}	605.6086
Volume of balloon membrane, [m^3]	V_{mem}	6.926168e-03
Mass of balloon membrane, [kg]	m_{mem}	6.649121
Density of air, [kg/m^3]	ρ_{air}	8.920266e-02
Speed of sound in air, [m/s]	a_{air}	291.6234
Atmospheric pressure, [Pa]	p_{air}	5417.677
Temperature of air, [K]	T_{air}	211.6189
Gradient of air density, [kg/m^2]	M_ρ	-1.576262e-05
Balloon added mass, [kg]	m_{ba}	27.01126
Bobbing frequency, [Hz]	f_{bob}	5.394984e-03

Table 3-1. Predicted properties of the balloon system at float altitude $z_f = 20486.96$ m.

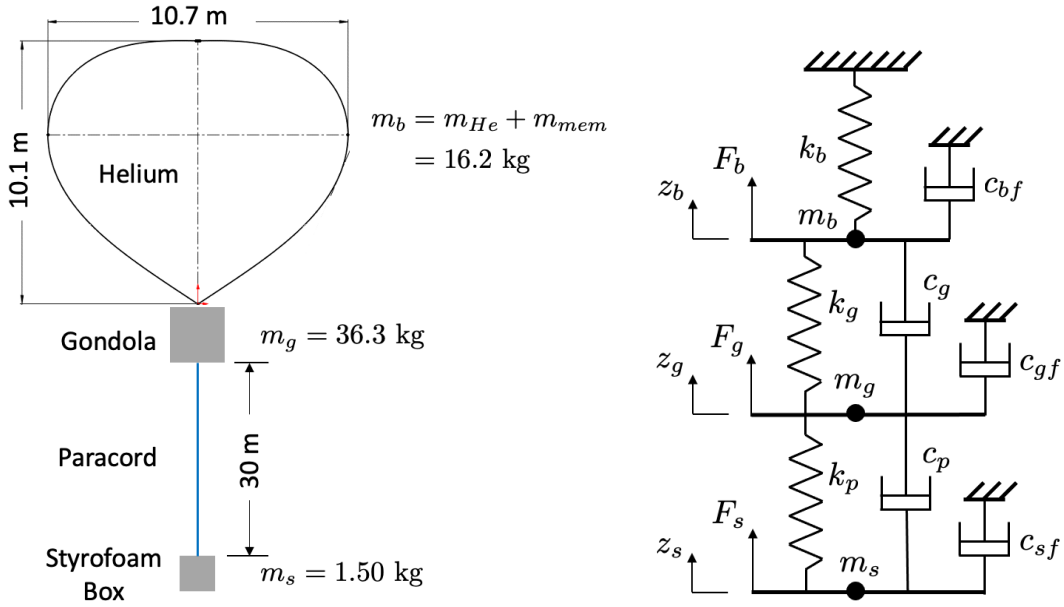

(a) Balloon system **(b)** Three degree of freedom model

Figure 3-2. Balloon system at float and the corresponding spring-mass-damper model.

Fig. 3-2b. Application of Newton's second law of motion to each mass gives the system of equations [8]

$$\begin{aligned}(m_b+m_{ba})\ddot{z}_b+(c_{bf}+c_g)\dot{z}_b-c_g\dot{z}_g+(k_g-gM_\rho V)z_b-k_gz_g&=F_b(t)\\(m_g+m_{ga})\ddot{z}_g-c_g\dot{z}_b+(c_{gf}+c_g+c_p)\dot{z}_g-c_p\dot{z}_s-k_gz_b+(k_g+k_s)z_g-k_pz_s&=F_g(t)\\(m_s+m_{sa})\ddot{z}_s-c_g\dot{z}_g+(c_{sf}+c_p)\dot{z}_s-k_pz_g+k_pz_s&=F_s(t),\end{aligned} \tag{3.16}$$

where $k_b = -gM_\rho V$ [N/m] is the buoyancy stiffness. The time argument for z_b, z_g and z_s has been omitted for clarity.

The stiffness of the Paracord is approximated using the stiffness of an equivalent length rod under axial load [8]

$$k_p = \frac{E_{para}\pi d_p^2}{4L_p}. \tag{3.17}$$

The stiffness of the balloon-gondola connection is approximated in the same manner using the Young's modulus for polyethylene E_{poly}, the distance between the center of gravity of the balloon and gondola L_{bg} and the diameter of the Paracord d_p:

$$k_g = \frac{E_{poly}\pi d_p^2}{4L_{bg}}. \tag{3.18}$$

To first order the gondola and styrofoam box are approximated as spheres. The added mass for each can then be computed using Eq. (3.12):

$$m_{ga} = \frac{\rho_{air} w_g d_g h_g}{2} \tag{3.19}$$

$$m_{sa} = \frac{\rho_{air} w_s d_s h_s}{2}. \tag{3.20}$$

The effective radius for the gondola and styrofoam box is then

$$r_g = \left(\frac{3 w_g d_g h_g}{4\pi}\right)^{1/3} \tag{3.21}$$

and

$$r_s = \left(\frac{3 w_s d_s h_s}{4\pi}\right)^{1/3}, \tag{3.22}$$

respectively, the radius of a sphere having the same volume.

The damping c_{bf}, c_{gf} and c_{sf} [N*s/m] accounts for the viscous drag experienced by the balloon, gondola and styrofoam box, respectively, during vertical oscillation about the float altitude. If the amplitude of the oscillations are small relative to the height of each component, the damping constant is given by [5]

$$c_f = 6\pi\mu r\left(1 + \frac{r}{\delta}\right) \tag{3.23}$$

where r is the effective radius, ω [rad/s] the radial frequency, μ the dynamic viscosity [Pa*s] and

$$\delta = \sqrt{\frac{2\mu}{\rho_{air}\omega}} \tag{3.24}$$

the radial depth into the fluid adjacent to the component where the viscous effects occur. At an altitude of 20 km and oscillation frequency of 2 Hz, $\delta \approx 5$ mm. The oscillation of the components also contributes to the added mass, however this contribution is insignificant relative to Eqs. (3.19) and (3.20). The damping constant c_p for the Paracord and c_g for the balloon-gondola

connection are unknown. These are determined later in Ch. 4 when comparing predictions to experimental data.

The governing equations (3.19) and (3.20) can be expressed in matrix form:

$$[M]\{\ddot{z}(t)\}+[C]\{\dot{z}(t)\}+[K]\{z(t)\}=\{F(t)\} \tag{3.25}$$

where

$$[M]=\begin{bmatrix} m_b+m_{ba} & 0 & 0 \\ 0 & m_g+m_{ga} & 0 \\ 0 & 0 & m_s+m_{sa} \end{bmatrix}, \tag{3.26}$$

$$[C]=\begin{bmatrix} c_{bf}+c_g & -c_g & 0 \\ -c_g & c_{gf}+c_g+c_p & -c_p \\ 0 & -c_g & c_{sf}+c_p \end{bmatrix}, \tag{3.27}$$

$$[K]=\begin{bmatrix} k_g-gM_\rho V & -k_g & 0 \\ -k_g & k_g+k_s & -k_p \\ 0 & -k_p & k_p \end{bmatrix}, \tag{3.28}$$

and

$$\{z(t)\}=\begin{Bmatrix} z_b(t) \\ z_g(t) \\ z_s(t) \end{Bmatrix} \qquad \{F(t)\}=\begin{Bmatrix} F_b(t) \\ F_g(t) \\ F_s(t) \end{Bmatrix}. \tag{3.29}$$

The undamped resonances of the system are determined from the homogenous form of these equations. Letting $[C]=[0]$, $\{F\}=\{0\}$ and substituting a time-harmonic response $\{z(t)\}=\{Z\}e^{i\omega t}$ gives the generalized eigenvalue problem

$$[K]=\{\omega^2\}[M]. \tag{3.30}$$

Using the parameters in Tables 2-1 and 3-1, the eigenvalue problem is solved using the MATLAB [6] function *eig* to obtain the vertical resonance frequencies

$$f_1=5.391760\text{e-}03 \text{ Hz} \qquad f_2=1.940965 \text{ Hz} \qquad f_3=3.776354 \text{ Hz}. \tag{3.31}$$

The lowest resonance is the bobbing frequency of the system previously given by Eq. (3.14). The corresponding mode shapes are shown in Fig. 3-3. The unperturbed location of the balloon, gondola and styrofoam box are indicated by the unfilled circles, the filled circles are the locations at one quarter cycle at the resonance frequency. Mode 1 is effectively a rigid body mode with all three masses moving in phase with constant separation distance. In mode 2 the balloon is out of phase with the gondola and styrofoam box, and in mode 3 the predominant movement is the styrofoam box with very slight out of phase motion of the gondola.

The resonance frequencies and mode shapes are used to determine the damping constants. The viscous damping associated with oscillatory motion, Eq. (3.23), is frequency dependent. The

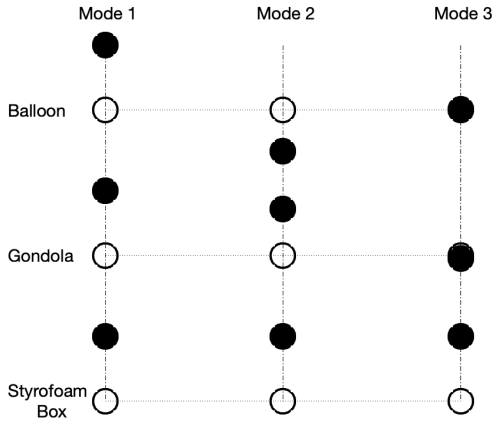

Figure 3-3. Modes shapes corresponding to resonance frequencies f_1, f_2 and f_3. The unperturbed location of the balloon, gondola and styrofoam box are indicated by the unfilled circles. The filled circles are their locations during a quarter cycle of the oscillation.

relative motion of the balloon and gondola is greatest for mode 2 and therefore a good assumption of their damping coefficients are

$$c_{bf} = 6\pi r_b\left(\mu + r_b\sqrt{\mu\rho_{air}\pi f_2}\right) \tag{3.32}$$

$$c_{gf} = 6\pi r_g\left(\mu + r_g\sqrt{\mu\rho_{air}\pi f_2}\right), \tag{3.33}$$

respectively, where r_b is the effective radius of the balloon given by Eq. (3.35). As frequency increases, so does the damping coefficient. Considering the motion of the styrofoam box in modes 2 and 3, an appropriate choice for the damping coefficient is

$$c_{sf} = 6\pi r_g\left(\mu + r_g\sqrt{\mu\rho_{air}\pi f_3}\right). \tag{3.34}$$

3.3. Infrasound to Net Force Relation

With the governing equations (3.16) for vertical motion developed, the next step is to derive a relation between the incident infrasound signal and the resulting forces on the balloon, gondola and styrofoam box. The infrasound signal will be modeled as a propagating plane wave. Each of the three components of the balloon system are approximated as a sphere of appropriate radius. The effective radius for the gondola and styrofoam box is given by Eq. (3.21) and (3.22), respectively. For the balloon envelope, the effective radius is obtained by equating the volume of the balloon in Eq. (3.4) with that of a sphere, giving

$$r_b = \frac{1}{2}\left(d_e^2 h_e\right)^{1/3}. \tag{3.35}$$

The total pressure, incident plus scattered, on the surface of a rigid, immoveable sphere due to an incident time-harmonic plane wave will now be derived. The corresponding net force is obtained

by integrating over the surface of the sphere. Since the balloon is filled with helium, the rigid assumption is not correct but is a sufficient result for the current developments. In future work, the correct pressure loading will be derived, taking into account the transmission of the infrasound through the balloon.

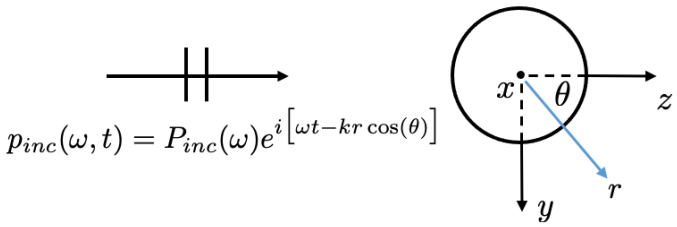

Figure 3-4. Propagating plane wave incident on rigid sphere.

Consider a time-harmonic plane wave incident upon a rigid sphere of radius a as shown in Fig. 3-4. The plane wave propagates along the z-axis from $-z$ to $+z$ with frequency dependent amplitude $P_{inc}(\omega)$. In Cartesian coordinates the incident plane wave is expressed

$$p_{inc}(\omega,r,\theta,t) = P_{inc}(\omega)e^{i\left[\omega t - kr\cos(\theta)\right]}, \tag{3.36}$$

where (r,θ) locates a point relative to the center of the sphere and $k = \omega/a_{air}$ [1/m] is the wavenumber.

Applying Eq. (10.1.47),

$$e^{iz\cos(\theta)} = \sum_{n=0}^{\infty}(2n+1)e^{\frac{1}{2}n\pi i}j_n(z)P_n(\cos(\theta)), \tag{3.37}$$

and Eq. (10.1.34),

$$j_n(ze^{m\pi i}) = e^{mn\pi i}j_n(z), \tag{3.38}$$

in Abramowitz and Stegun [1], the incident plane wave in Eq. (3.36) can be expressed in the spherical coordinate system:

$$p_{inc}(\omega,r,\theta) = P_{inc}(\omega)\sum_{n=0}^{\infty}(2n+1)(-i)^n j_n(kr)P_n(\cos(\theta)) \tag{3.39}$$

where $j_n(kr) = \sqrt{\frac{\pi}{2kr}}J_{n+\frac{1}{2}}(kr)$ is the spherical Bessel function of the first kind and $P_n(\cos(\theta))$ is the Legendre polynomial. The time-harmonic multiplier $e^{i\omega t}$ has been omitted.

The unknown scattered pressure is expressed in the general form

$$p_{scat}(\omega,r,\theta) = \sum_{n=0}^{\infty}\sum_{m=0}^{n}A_{mn}h_n^{(2)}(kr)P_n^m(\cos(\theta))e^{im\phi} \tag{3.40}$$

where $P_n^m(\cos(\theta))$ is the associated Legendre function for $m \neq 0$,

$$h_n^{(2)}(kr) = j_n(kr) + iy_n(kr) \tag{3.41}$$

is the spherical Bessel function of the third kind, and $y_n(kr) = \sqrt{\frac{\pi}{2kr}} Y_{n+\frac{1}{2}}(kr)$ the spherical Bessel function of the second kind. Equation (3.40) describes spherically spreading waves radiating away from the center of the sphere in Fig. 3-4.

The total pressure and total particle velocity at any point in the fluid is the sum of the incident and scattered fields

$$p_{tot}(\omega, r, \theta) = p_{inc}(\omega, r, \theta) + p_{scat}(\omega, r, \theta) \tag{3.42}$$

$$\vec{u}_{tot}(\omega, r, \theta) = \vec{u}_{inc}(\omega, r, \theta) + \vec{u}_{scat}(\omega, r, \theta). \tag{3.43}$$

With the sphere assumed to be rigid and unmovable, the radial component of the total particle velocity at the surface, $r = a$, must equal zero and therefore

$$u_{r,scat}(\omega, r, \theta)\big|_{r=a} = -u_{r,inc}(\omega, r, \theta)\big|_{r=a}. \tag{3.44}$$

Hence the amplitude of the scattered field can be easily determined from that of the incident field.

The incident and scattered radial particle velocity is obtained from Eqs. (3.39) and (3.40) by applying the momentum equation

$$\rho_{air} \frac{\partial u_r}{\partial t} = -\frac{\partial p}{\partial r} \tag{3.45}$$

giving

$$u_{r,inc} = \frac{iP_{inc}(\omega)}{\omega \rho_{air}} \sum_{n=0}^{\infty} (2n+1)(-i)^n j_n'(kr) P_n(\cos(\theta)) \tag{3.46}$$

$$u_{r,scat} = \frac{i}{\omega \rho_{air}} \sum_{n=0}^{\infty} \sum_{m=0}^{n} A_{mn} h_n^{(2)\prime}(kr) P_n^m(\cos(\theta)) e^{im\phi} \tag{3.47}$$

where the derivative of the Bessel functions with respect to their argument is indicated by the superscript $'$.

Substitution of these expressions into Eq. (3.44) and invoking the orthogonality of the complex exponential and the Legendre polynomial [3] finds $m = 0$ and

$$A_{0n} = \frac{-P_{inc}(2n+1)(-i)^n j_n'(ka)}{h_n^{(2)\prime}(ka)}. \tag{3.48}$$

Substituting this result into Eq. (3.40) gives for the scattered pressure

$$p_{scat}(\omega, r, \theta) = -P_{inc}(\omega) \sum_{n=0}^{\infty} (2n+1)(-i)^n j_n'(ka) \frac{h_n^{(2)}(kr)}{h_n^{(2)\prime}(ka)} P_n(\cos(\theta)). \tag{3.49}$$

The total surface pressure is the sum of this result and the incident pressure in Eq. (3.39) evaluated at the surface of the sphere $r = a$

$$p_{tot}(\omega, a, \theta) = P_{inc}(\omega) \sum_{n=0}^{\infty} (2n+1)(-i)^n P_n(\cos(\theta)) \frac{\left[j_n(ka) h_n^{(2)\prime}(ka) - j_n'(ka) h_n^{(2)}(ka) \right]}{h_n^{(2)\prime}(ka)}. \tag{3.50}$$

The bracketed term can be simplified by first expanding it using Eq. (3.41):

$$j_n(ka)h_n^{(2)\prime}(ka) - j_n'(ka)h_n^{(2)}(ka) = i\Big[j_n'(ka)y_n(ka) - j_n(ka)y_n'(ka)\Big]. \tag{3.51}$$

Applying the recurrence relation Eq. (10.1.20),

$$f_n'(z) = \frac{n}{2n+1}f_{n-1}(z) - \frac{n+1}{2n+1}f_{n+1}(z), \tag{3.52}$$

and Eq. (10.1.31),

$$j_n(z)y_{n-1}(z) - j_{n-1}(z)y_n(z) = \frac{1}{z^2}, \tag{3.53}$$

in [1] finds

$$j_n(ka)h_n^{(2)\prime}(ka) - j_n'(ka)h_n^{(2)}(ka) = -\frac{i}{k^2a^2}. \tag{3.54}$$

The total pressure on the surface of the sphere is then finally

$$p_{tot}(\omega,a,\theta) = \frac{P_{inc}(\omega)}{k^2a^2}\sum_{n=0}^{\infty}\frac{(2n+1)(-i)^{n+1}}{h_n^{(2)\prime}(ka)}P_n(\cos(\theta)). \tag{3.55}$$

The total pressure on the surface of the sphere produces a net force causing the sphere to move. This force is obtained by integrating over the spherical surface. The differential force directed into the sphere at surface location (θ,ϕ) is given by the product of the total pressure, the unit vector, and the solid angle $a^2\sin(\theta)d\theta d\phi$. The unit vector directed outward from the center of the sphere can be described in spherical coordinates as

$$\hat{e}_r(\theta,\phi) = \cos(\phi)\sin(\theta)\hat{e}_x + \sin(\phi)\cos(\theta)\hat{e}_y + \cos(\theta)\hat{e}_z. \tag{3.56}$$

Integrating over the entire surface gives the net force

$$\vec{F}_{net} = -\hat{e}_z\int_0^{2\pi}\int_0^{\pi}p_{tot}(\omega,a,\theta)\hat{e}_r(\theta,\phi)a^2\sin(\theta)d\theta d\phi. \tag{3.57}$$

Since the total surface pressure is axially symmetric about the z-axis, integration over ϕ is straightforward giving

$$\vec{F}_{net} = -\hat{e}_z\frac{2\pi P_{inc}}{k^2}\sum_{n=0}^{\infty}\frac{(2n+1)(-i)^{n+1}}{h_n^{(2)\prime}(ka)}\int_0^{\pi}P_n(\cos(\theta))\sin(\theta)\cos(\theta)d\theta. \tag{3.58}$$

To evaluate the integral, substitute $v = \cos(\theta)$ giving

$$\int_{-1}^{1}P_n(v)v dv. \tag{3.59}$$

This is evaluated using the orthogonality of the Legendre polynomials

$$\int_{-1}^{1}P_n(v)P_m(v)dv = \begin{cases}0 & m\neq n\\ \frac{2}{2n+1} & m=n\end{cases} \tag{3.60}$$

By definition $P_1(v) = v$ and therefore

$$\int_{-1}^{1} P_n(v)P_1(v)dv = \begin{cases} 0 & n \neq 1 \\ \frac{2}{3} & n = 1 \end{cases} \tag{3.61}$$

Therefore only the $n = 1$ term contributes to the net force on the sphere. For all other values of n the variation of total pressure over the surface produces a net force of zero. Substituting the result of Eq. (3.61) for the integral in Eq. (3.58) gives the net force

$$\vec{F}_{net}(\omega) = \frac{4\pi P_{inc}(\omega)}{k^2 h_1^{(2)\prime}(ka)} \hat{e}_z. \tag{3.62}$$

A vector transfer function $\vec{H}(\omega)$ [m^2] relating the amplitude of the incident plane wave to the force is constructed from this result

$$\vec{H}(\omega) \equiv \frac{\vec{F}_{net}(\omega)}{P_{inc}(\omega)} = \frac{4\pi}{k^2 h_1^{(2)\prime}(ka)} \hat{e}_z. \tag{3.63}$$

The real and imaginary components of the transfer function for the balloon, gondola and styrofoam box are plotted in Fig. 3-5 for the frequency bandwidth of the recorded infrasound signals. Considering a unit amplitude infrasound signal at each frequency, the resulting force for all three is predominately in phase quadrature with the pressure. Further, due to their small size relative to the range of wavelengths of the infrasound, the resulting force on the gondola and styrofoam box are orders of magnitude smaller than that of the balloon.

3.4. Estimating Vertical Forces

The resulting force on each balloon component is estimated by convolving the infrasound signal measured by the microbarometer with the transfer function in Eq. (3.63). The convolution is performed in the frequency domain using the fast Fourier transform and the resulting force is inverse transformed back to the time domain.

The infrasound signal measured by the microbarometer for each subevent is shown in Fig. 3-6. An overall window of 30 seconds in length as well as a zoom of the main infrasound signal is provided. The data shown is the result of detrending the measured data using a least-squares fit of a quartic polynomial to remove the slow variation of atmospheric pressure over time. Events 1 and 2 shown a strong N-wave associated with the shock wave from the ground explosion followed by decaying reverberation. The auto-spectral density of the overall microbarometer signals in Figs. 3-6 are shown in Fig. 3-7. For all four events there is a peak in the infrasound signal at approximately 3 Hz.

The vertical component of the force applied to the balloon, gondola and styrofoam box is obtained by convolution. The transfer functions in Fig. 3-5 are multiplied by the microbarometer signals for each event in Fig. 3-7 and the vertical component obtained using the incidence angle:

$$F(\omega) = \vec{H}(\omega)P_{inc}(\omega)\cos(\theta_{ele})\hat{e}_z \tag{3.64}$$

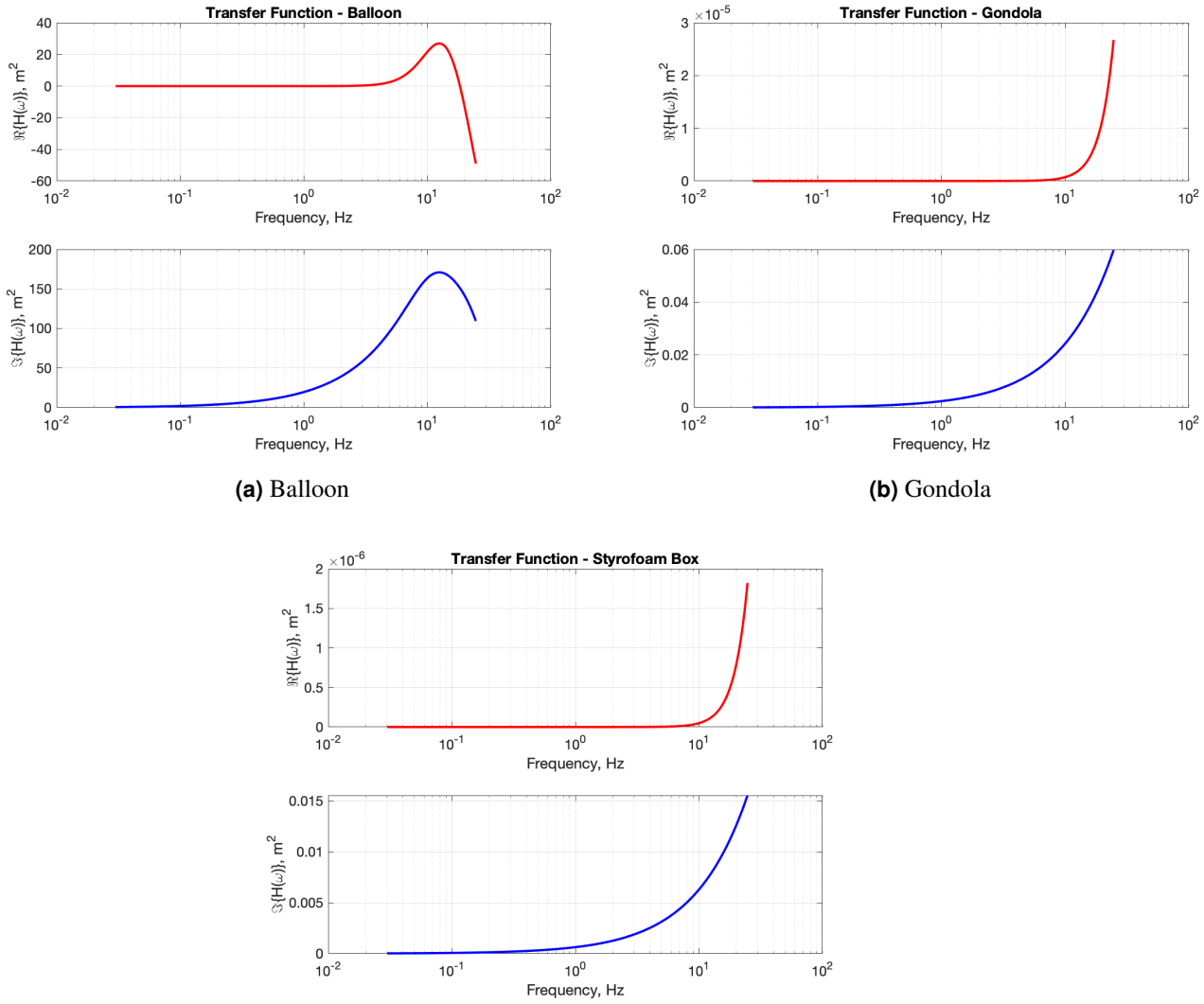

(a) Balloon

(b) Gondola

(c) Styrofoam Box

Figure 3-5. Real (red) and imaginary (blue) components of the transfer function for the (a) balloon, (b) gondola and (c) styrofoam box.

where θ_{ele} is angle of arrival of the infrasound signal, measured from vertical ($+z$). As this is a proof of concept investigation, the arrival angle was determined from ray tracing analysis using the known location of the source and location of the balloon.

The resulting vertical forces are inverse Fourier transformed back to the time domain. The estimated forces on the ballon (red), gondola (green) and styrofoam instrumentation box(blue) for Events 1 and 2 are plotted in Fig. 3-8. As expected from the transfer functions in Fig. 3-5, the force on the balloon is significantly larger relative to the force on the gondola and styrofoam box.

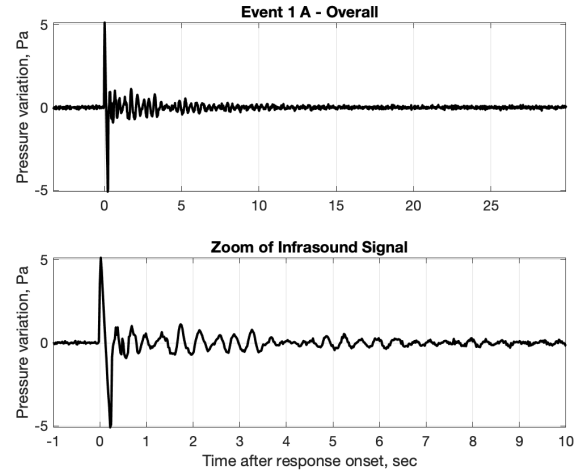

(a) Event 1-A

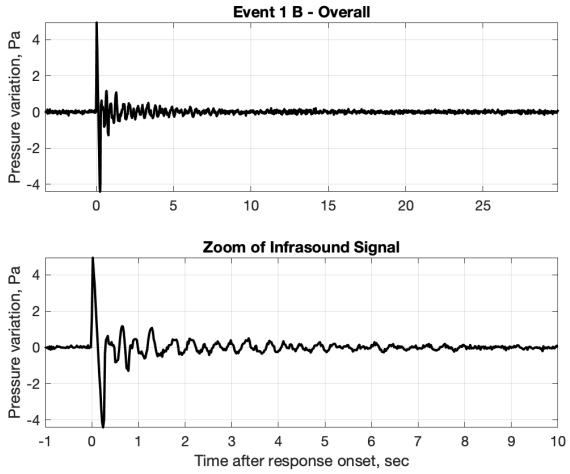

(b) Event 1-B

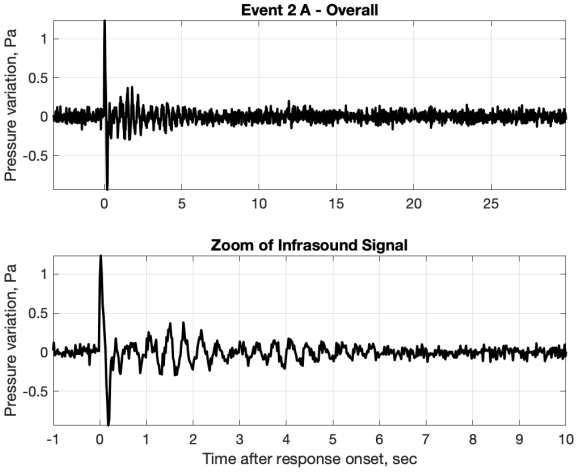

(c) Event 2-A

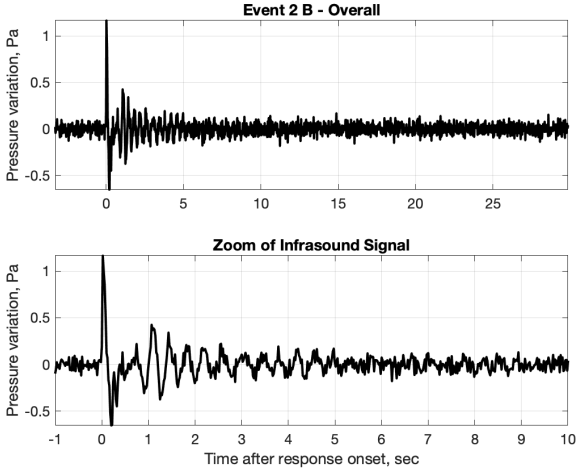

(d) Event 2-B

Figure 3-6. Detrended infrasound signal measured by the microbarometer in the styrofoam instrumentation box. The overall signal is 30 seconds long and the zoom shows the specific detail of the infrasound signal.

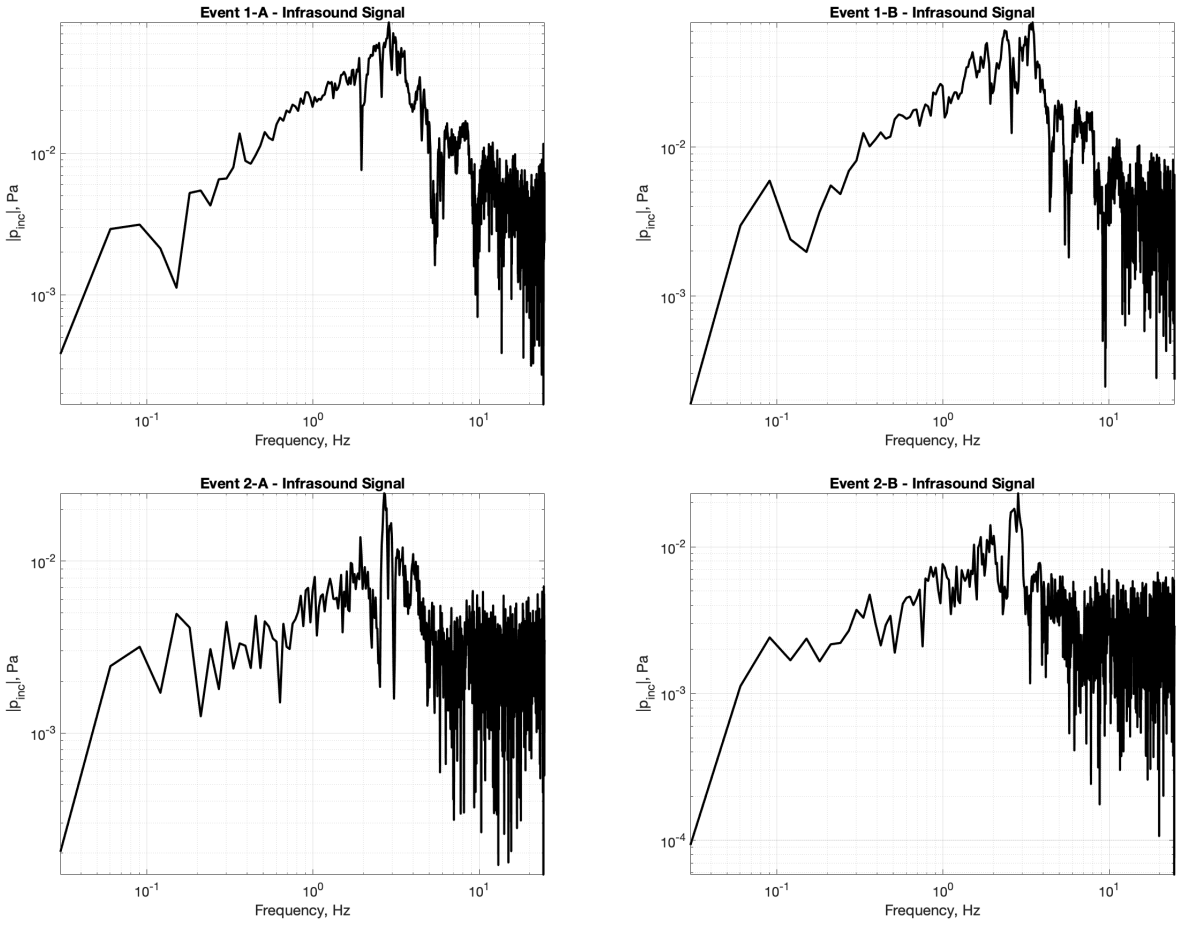

Figure 3-7. Auto-spectral density of the 30 second of microbarometer time histories in Fig. 3-6.

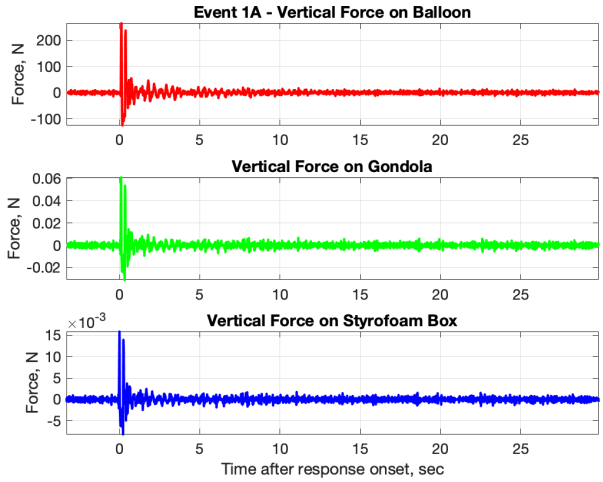

(a) Event 1-A

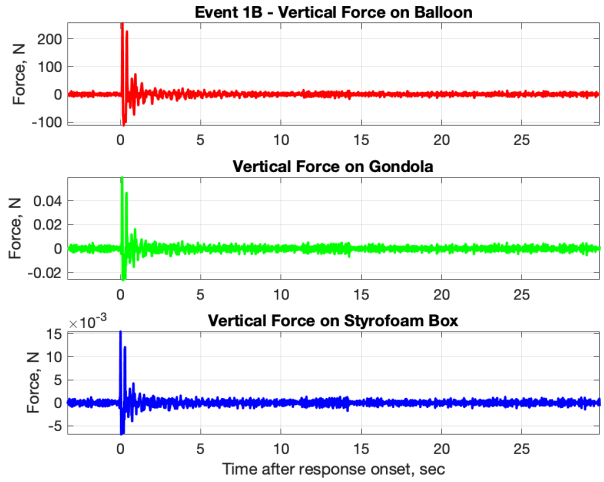

(b) Event 1-B

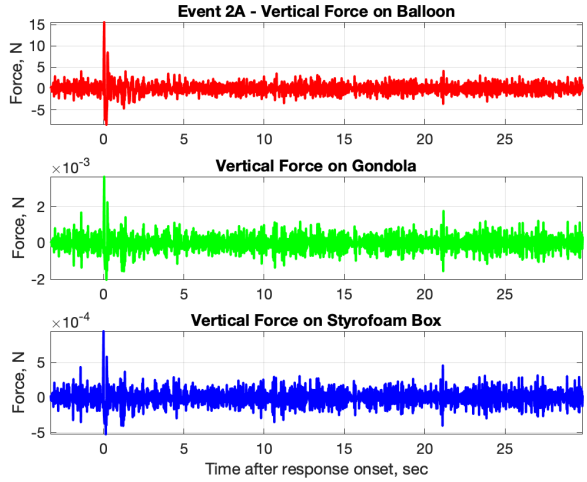

(c) Event 2-A

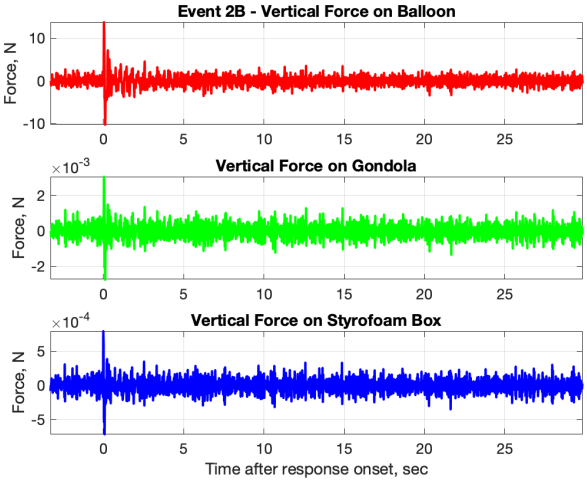

(d) Event 2-B

Figure 3-8. Estimated forces on the balloon, gondola and styrofoam box for Events 1 and 2.

4. PREDICTION OF VERTICAL RESPONSE

The vertical response of the balloon, gondola and styrofoam box is obtained by integrating the governing equations (3.16) using the corresponding forces in Fig. 3-8. The governing equations are numerically integrated in MATLAB using the function *ode89* which uses 8^{th} and 9^{th} order Runge-Kutta formulas.

To apply Runge-Kutta integration, the system of second-order governing equations are converted to an equivalent system of first-order equations. This is accomplished by making the substitution

$$\begin{aligned} z_1(t) &= z_b(t) \\ z_2(t) &= \dot{z}_b(t) \\ z_3(t) &= z_g(t) \\ z_4(t) &= \dot{z}_g(t) \\ z_5(t) &= z_s(t) \\ z_6(t) &= \dot{z}_s(t) \end{aligned} \tag{4.1}$$

into Eqs. (3.16) giving

$$\begin{aligned} (m_b+m_{ba})\dot{z}_2+(c_{bf}+c_g)z_2-c_gz_4+(k_g-gM_\rho V)z_1-k_gz_3 &= F_b(t) \\ (m_g+m_{ga})\dot{z}_4-c_gz_2+(c_{gf}+c_g+c_p)z_4-c_pz_6-k_gz_1+(k_g+k_s)z_3-k_pz_5 &= F_g(t) \\ (m_s+m_{sa})\dot{z}_6-c_gz_4+(c_{sf}+c_p)z_6-k_pz_3+k_pz_5 &= F_s(t). \end{aligned} \tag{4.2}$$

Dividing through by the mass coefficient and rearranging gives

$$\begin{aligned} \dot{z}_1(t) &= z_2(t) \\ \dot{z}_2(t) &= -\frac{k_g-gM_\rho V}{m_b+m_{ba}}z_1-\frac{c_{bf}+c_g}{m_b+m_{ba}}z_2+\frac{k_g}{m_b+m_{ba}}z_3+\frac{c_g}{m_b+m_{ba}}z_4+\frac{F_b(t)}{m_b+m_{ba}} \\ \dot{z}_3(t) &= z_4(t) \\ \dot{z}_4(t) &= \frac{k_g}{m_g+m_{ga}}z_1+\frac{c_g}{m_g+m_{ga}}z_2-\frac{k_g+k_s}{m_g+m_{ga}}z_3-\frac{c_{gf}+c_g+c_p}{m_g+m_{ga}}z_4+\frac{k_p}{m_g+m_{ga}}z_5+ \\ &\quad \frac{c_p}{m_g+m_{ga}}z_6+\frac{F_g(t)}{m_g+m_{ga}} \\ \dot{z}_5(t) &= z_6(t) \\ \dot{z}_6(t) &= \frac{k_p}{m_s+m_{sa}}z_3+\frac{c_g}{m_s+m_{sa}}z_4-\frac{k_p}{m_s+m_{sa}}z_5-\frac{c_{sf}+c_p}{m_s+m_{sa}}z_6+\frac{F_s(t)}{m_s+m_{sa}}. \end{aligned} \tag{4.3}$$

with initial conditions $z_1(0) = z_3(0) = z_5(0) = 0$ for zero initial displacement and $z_2(0) = z_4(0) = z_6(0) = 0$ for zero initial velocity. This is the form used in MATLAB.

The infrasound signal does not arrive at the balloon, gondola and styrofoam box simultaneously unless the angle of arrival $\theta_{ele} = \pi/2$ (i.e. the infrasound is propagating parallel to the horizon). Since the microbarometer was located in the styrofoam box, the forces F_b and F_g for the ballon and gondola must be time-shifted to account for the vertical travel time and for time-alignment between the predicted acceleration response and the experimental measurement. It is assumed the variations in sound speed between the location of the styrofoam box and balloon are negligible. For arrival angle θ_{ele}, the propagation speed in the vertical direction is $a_v = \cos(\theta_{ele})/a_{air}$ where a_{air} is the propagation speed of the infrasound signal. The arrival time at the balloon t_b and the gondola t_g are then

$$t_g = t_s + \frac{L_p}{a_{air}} \cos(\theta_{ele}) \tag{4.4}$$

$$t_b = t_s + \frac{L_{bg} + L_p}{a_{air}} \cos(\theta_{ele}) \tag{4.5}$$

where t_s is the arrival time at the styrofoam box which is assumed to be $t_s = 0$, time of the onset of response. Therefore in Eqs. (4.3)

$$F_g(t) = F_g(t)H(t - t_g) \tag{4.6}$$

$$F_b(t) = F_b(t)H(t - t_b) \tag{4.7}$$

where H is the Heaviside unit step function.

4.1. Event 1

The time-domain acceleration of the styrofoam box was predicted using the estimated forces plotted in Fig. 3-6a with damping coefficients $c_g = c_p = 0$. The values for the damping coefficients c_g and c_p were determined by visual inspection. The experimental and the predicted accelerations were converted to the frequency domain and their normalized auto-spectral density compared in Fig. 4-1. The second and third resonances of the balloon system at approximately $f_2 = 1.9$ and $f_3 = 3.7$ Hz are clearly visible in the predicted acceleration, with good agreement with the two dominant peaks in the experimental acceleration. This indicates the spring constants k_g and k_p are sufficiently accurate.

The value of the damping coefficients c_g and c_p were adjusted until agreement with the experimental acceleration was achieved. In Fig. 4-2 is shown the experimental and predicted accelerations with $c_g = 15$ and $c_p = 2.3$ [N*s/m]. Good agreement is achieved in the frequency region around the two resonances of the system. These values for c_g and c_p were used for all predictions of balloon system response for Event 1.

The predicted time-domain acceleration of the styrofoam box is compared to the experimental acceleration for Event 1-A in Fig. 4-3. The predicted acceleration is plotted with the amplitude inverted (multiplied by -1) to overlay the experimental data. The cause of the inversion in the

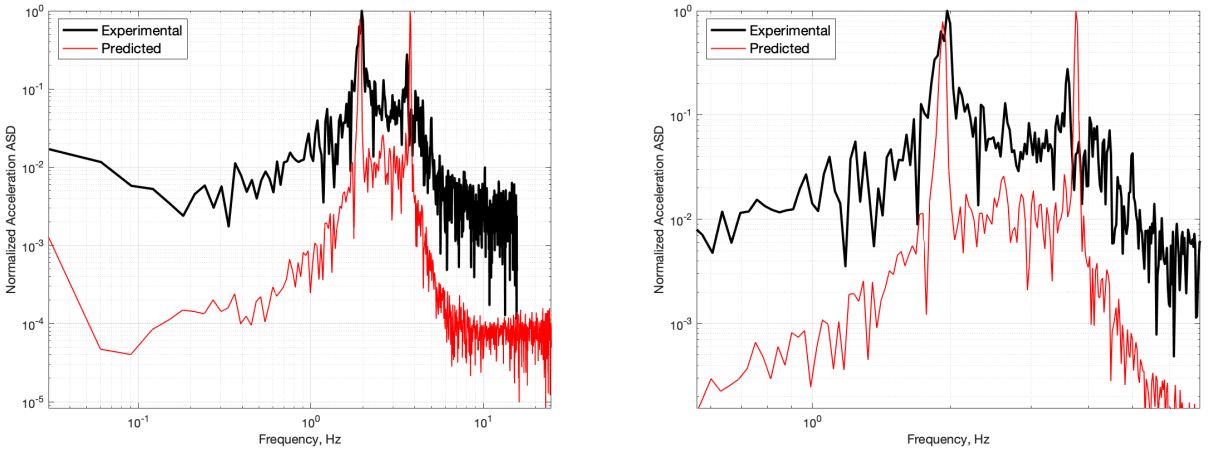

(a) Overall **(b)** Zoom into peaks

Figure 4-1. Auto-spectral density of experimental (black) and predicted (red) acceleration of styrofoam box for Event 1-A. The damping coefficients c_g and c_p are zero for the predicted acceleration.

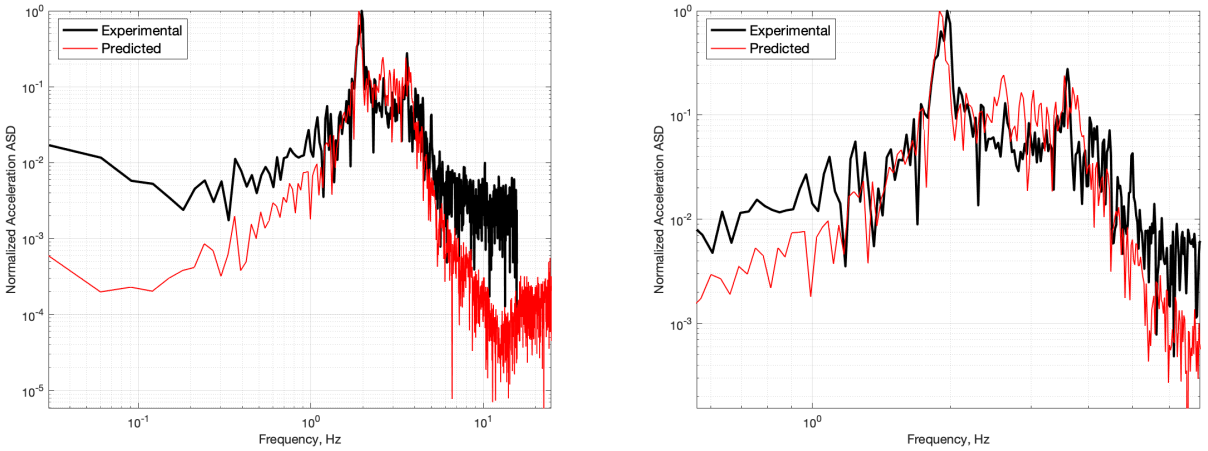

(a) Overall **(b)** Zoom into peaks

Figure 4-2. Auto-spectral density of experimental (black) and predicted (red) acceleration of styrofoam box for Event 1-A. The damping coefficients $c_g = 15$ and $c_p = 2.3$ [N*s/m] for the predicted acceleration.

experimental data is unknown, and would imply the initial displacement of the styrofoam box was downward, toward the incident infrasound signal which seems counterintuitive. In Fig. 4-3a the amplitude of both accelerations are normalized by the maximum value of acceleration during the time window. There is good agreement with the experimental data with alignment in the dominant frequency of oscillation. There is a slight excess of attenuation in the predicted acceleration in the 1 to 3 sec. region.

In Fig. 4-3b the actual acceleration is plotted. The amplitude of the forcing on the balloon was adjusted to $0.73F_b$ to achieve good agreement; F_g and F_s were not adjusted. This adjustment was

expected as the balloon was assumed perfectly rigid which is not the case since it is filled with helium. Based upon the phase speed and density of the helium and the air at float altitude as listed in Table 3-1 the reflection coefficient of the balloon envelope (neglecting the influence of the membrane) is

$$R = \frac{\rho_{He} a_{He} - \rho_{air} a_{air}}{\rho_{He} a_{He} + \rho_{air} a_{air}} \tag{4.8}$$

$$= -0.3149169 \tag{4.9}$$

where the negative value is due to the impedance of the helium being less than that of the air. Therefore an incident plane wave would reflect out of phase with the amplitude reduced by 31.5% and the total pressure at the surface would be 69.5% relative to a rigid sphere. This agrees well with the adjusted forcing of $0.73F_b$ used for Fig. 4-3b.

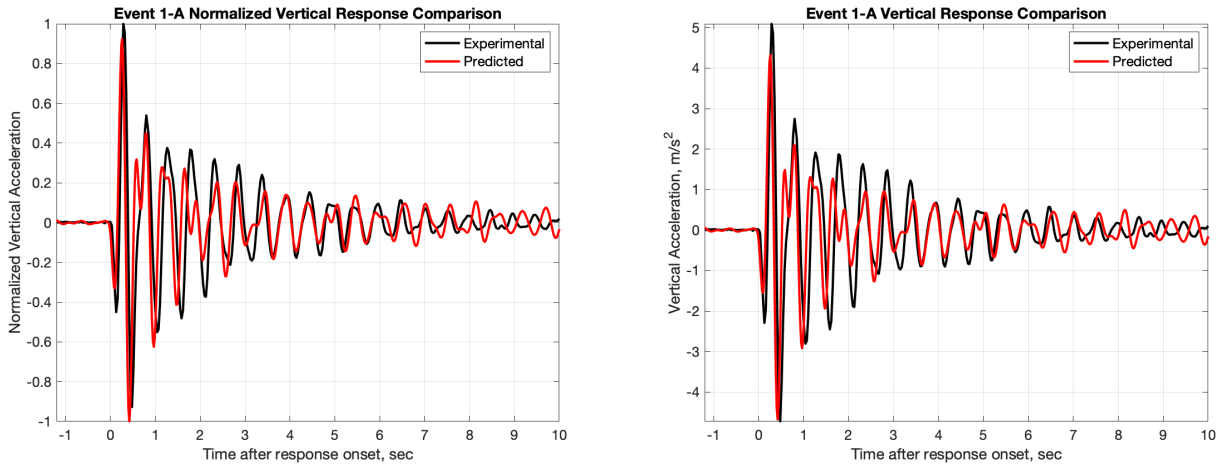

(a) Normalized Acceleration

(b) Actual Acceleration

Figure 4-3. Comparison of experimental (black) and predicted (red) acceleration of the styrofoam box for Event 1-A. The amplitude in (a) is normalized by the maximum value, (b) the force on the ballon is $0.73F_b$.

The predicted vertical displacement, velocity and acceleration of the balloon (red), gondola (green) and styrofoam box (blue) are shown in Fig. 4-4. The maximum displacement of the three components are small, in the 10 to 20 mm range. The initial displacement of each is upward, in the direction of the infrasound propagation. Notice the displacement of the balloon leads the gondola which leads the styrofoam box, resulting from the time required for the balloon impulse to travel to the styrofoam box. The acceleration is shown as predicted (not inverted). The acceleration of the balloon follows closely the applied force in Fig. 3-8a.

The predicted acceleration of the styrofoam box for Event 1-B is compared to the experimental acceleration in Fig. 4-5. The damping coefficients c_g and c_p are those determined for Event 1-A and the predicted force on the ballon is $0.73F_b$. There is good agreement with the experimental data though again there is slight excess attenuation in the 1.5 to 3.5 sec. region.

The predicted vertical displacement, velocity and acceleration of the balloon (red), gondola (green) and styrofoam box (blue) for Event 1-B are shown in Fig. 4-6. The first resonance

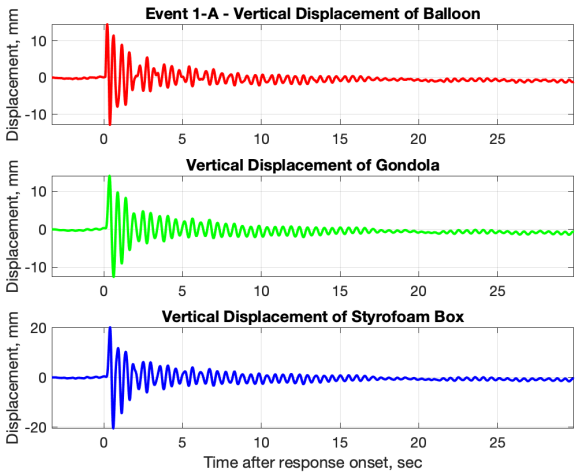

(a) Displacement

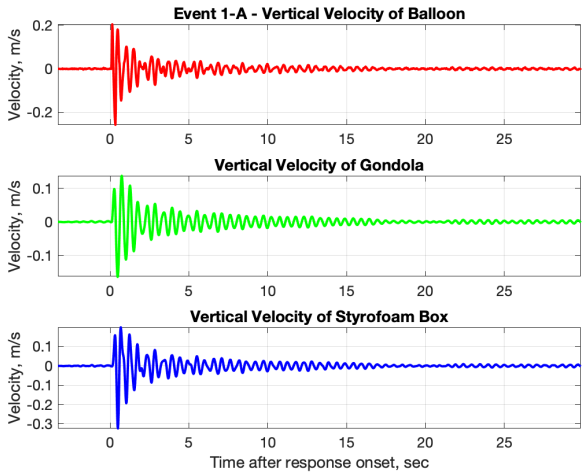

(b) Velocity

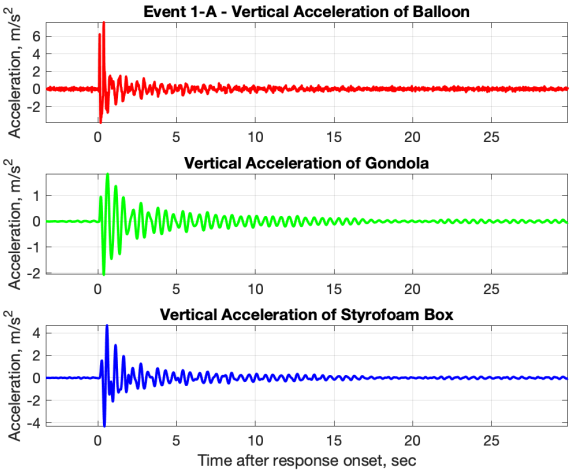

(c) Acceleration

Figure 4-4. Predicted response of the balloon, gondola and styrofoam box for Event 1-A: (a) displacement (in mm), (b) velocity and (c) acceleration.

(bobbing) mode is visible in the displacement. The velocity and acceleration are similar to those predicted for Event 1-A. This is expected as the microbarometer measurements for Event 1-A and 1-B in Fig. 3-7 are very similar.

4.2. Event 2

The normalized predicted and experimental acceleration auto-spectral densities for Event 2-A are shown in Fig. 4-7. The damping coefficients $c_g = c_p = 0$. Comparing the location of the second and third resonances, it appears the balloon system has become stiffer relative to Event 1. Increasing the Young's modulus of the Paracord by 20% to $E_{para} = 2.39 \times 10^9$ Pa and the

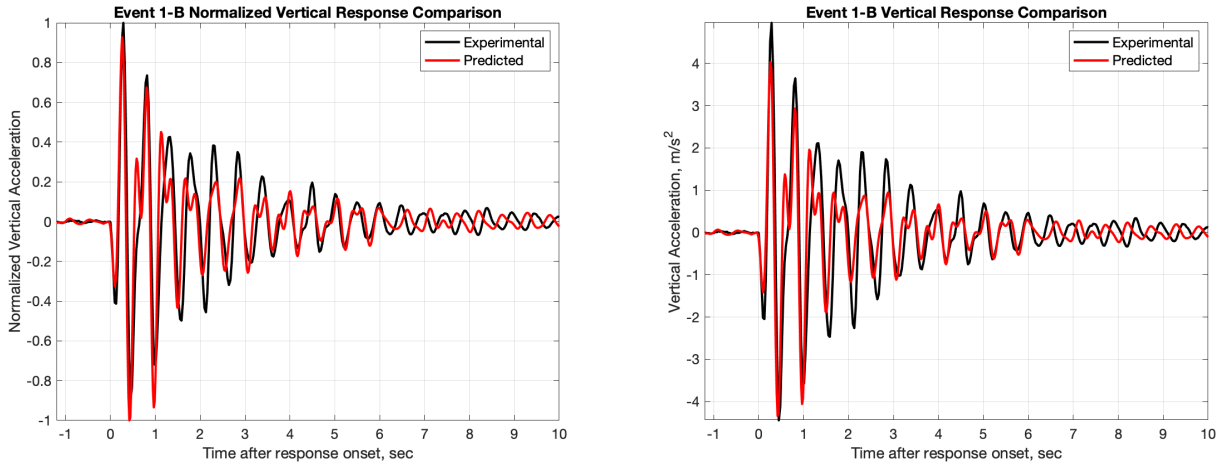

(a) Normalized Acceleration **(b)** Actual Acceleration

Figure 4-5. Comparison of experimental (black) and predicted (red) acceleration of the styrofoam box for Event 1-B. The amplitude in (a) is normalized by the maximum value, (b) the force on the ballon is $0.73F_b$.

modulus for the polyethylene balloon envelope 15% to $E_{poly} = 1.265 \times 10^9$ Pa gives better alignment with the experimental acceleration as shown in Fig. 4-8. To align the predicted with the experimental acceleration in the region around the two resonances, the damping coefficient values $c_g = 15$ and $c_p = 3.0$ were used. The Paracord is 30% more lossy compared to Event 1. The atmospheric conditions for Event 1 and 2 are nearly identical and the source of the increased stiffness and damping the system is unknown. Perhaps the solar radiation has modified the material properties.

The predicted time-domain acceleration of the styrofoam box is compared to the experimental measurement in Fig. 4-9. The predicted acceleration is again inverted to align with the experimental data. The normalized acceleration shown in Fig. 4-9a agrees well with the experimental data with an overshoot in response around 1.5 sec. The acceleration in Fig. 4-9b was predicted for a scaled balloon force of $0.73F_b$ as was done for Event 1. Fairly good agreement is achieved.

The predicted displacement, velocity and acceleration of the balloon (red), gondola (green) and styrofoam box (blue) for Event 2-A are shown in Fig. 4-10. As with Event 1-B, the displacement indicates the lowest mode (bobbing) is excited.

The predicted time-domain acceleration of the styrofoam box for Event 2-B is compared to the experimental measurement in Fig. 4-9. The predicted acceleration is again inverted to align with the experimental data. Good agreement is observed similar to Event 2-A.

The predicted displacement, velocity and acceleration of the balloon (red), gondola (green) and styrofoam box (blue) for Event 2-B are shown in Fig. 4-12. The displacement, velocity and acceleration response are similar to Event 2-A.

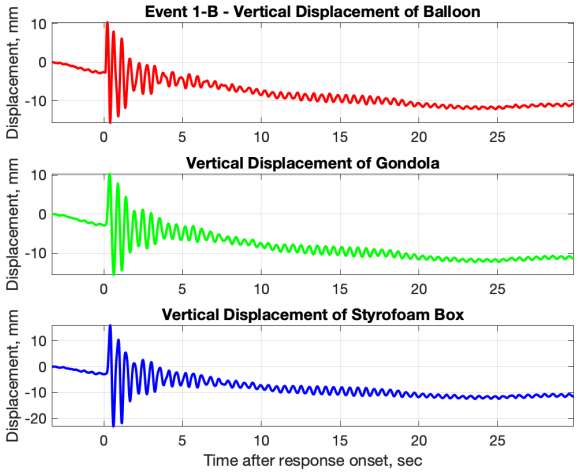

(a) Displacement

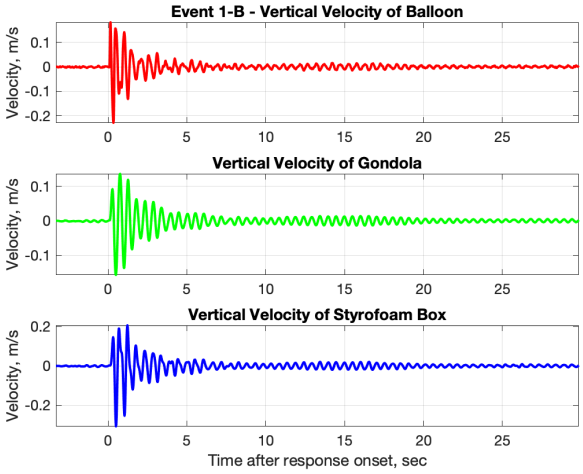

(b) Velocity

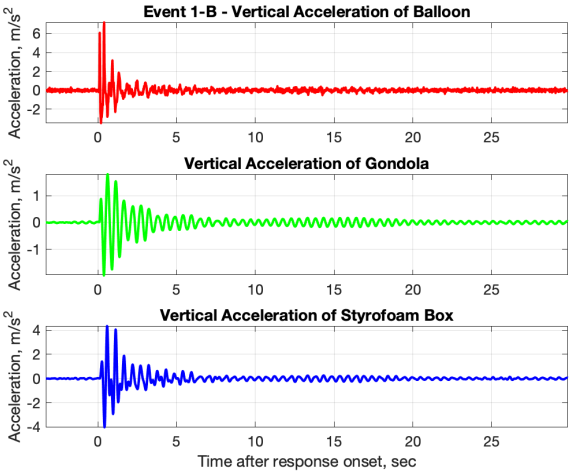

(c) Acceleration

Figure 4-6. Predicted response of the balloon, gondola and styrofoam box for Event 1-B: (a) displacement (in mm), (b) velocity and (c) acceleration.

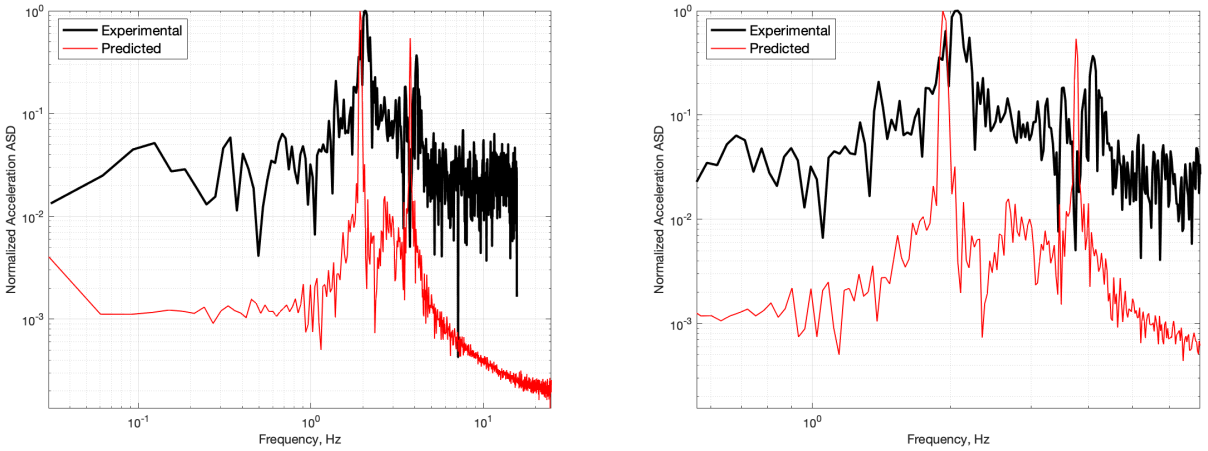

(a) Overall **(b)** Zoom into peaks

Figure 4-7. Auto-spectral density of experimental (black) and predicted (red) acceleration of styrofoam box for Event 2-A. The damping coefficients c_g and c_p are zero for the predicted acceleration.

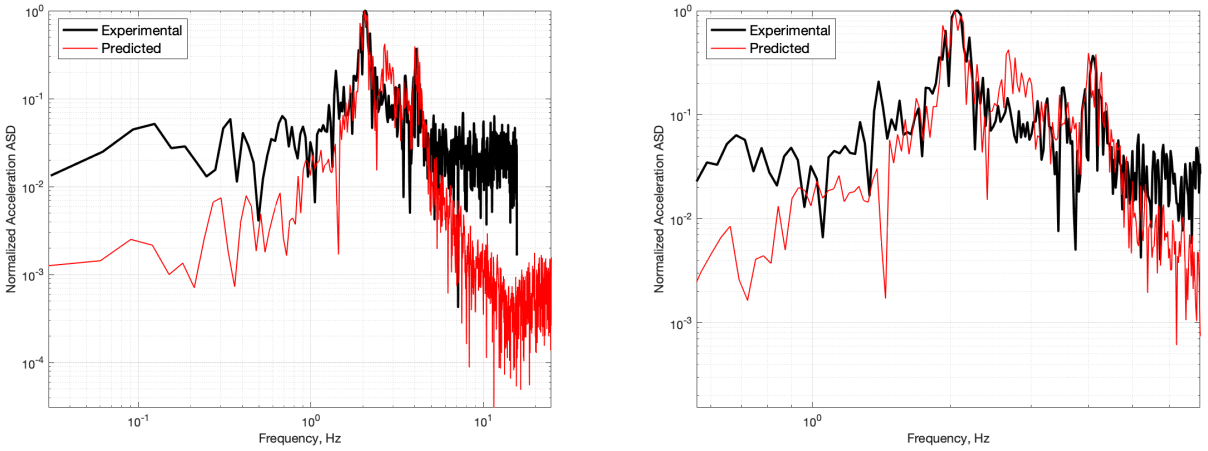

(a) Overall **(b)** Zoom into peaks

Figure 4-8. Auto-spectral density of experimental (black) and predicted (red) acceleration of styrofoam box for Event 2-A. The damping coefficients $c_g = 15$ and $c_p = 3$ [N*s/m] for the predicted acceleration.

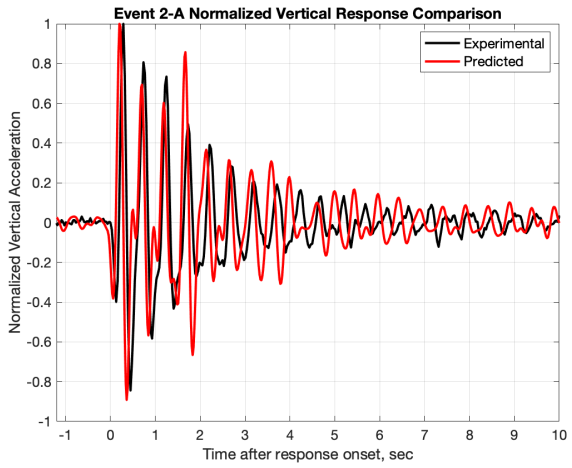

(a) Normalized Acceleration

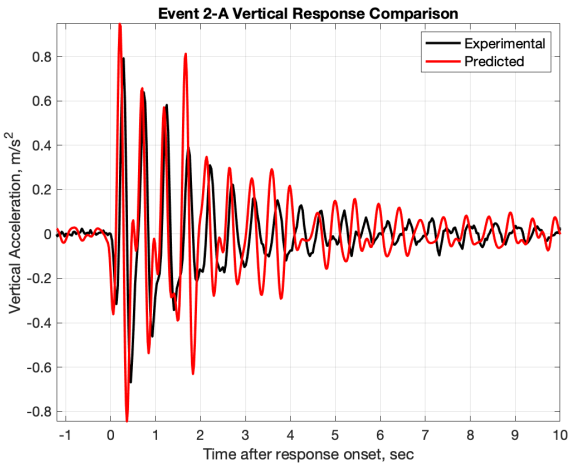

(b) Actual Acceleration

Figure 4-9. Comparison of experimental (black) and predicted (red) acceleration of the styrofoam box for Event 2-A. The amplitude in (a) is normalized by the maximum value, (b) the force on the ballon is $0.73F_b$.

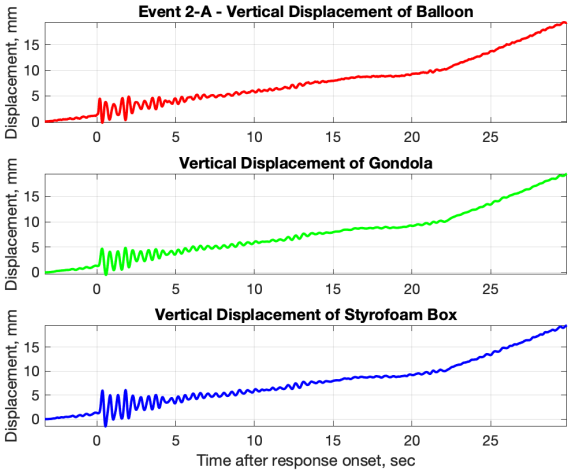

(a) Displacement

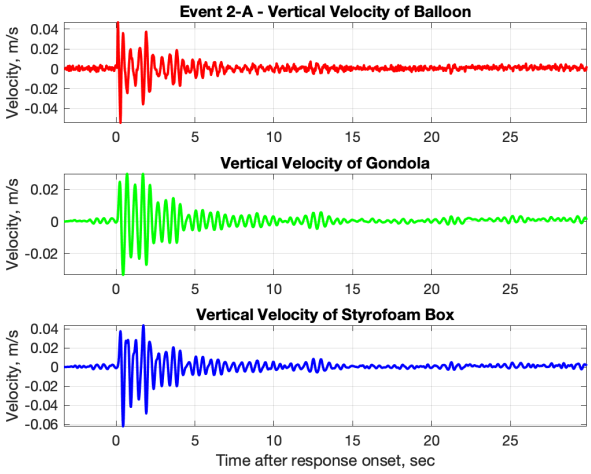

(b) Velocity

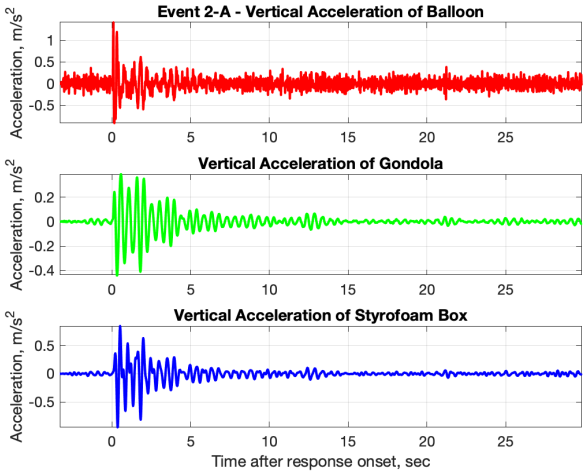

(c) Acceleration

Figure 4-10. Predicted response of the balloon, gondola and styrofoam box for Event 2-A: (a) displacement (in mm), (b) velocity and (c) acceleration.

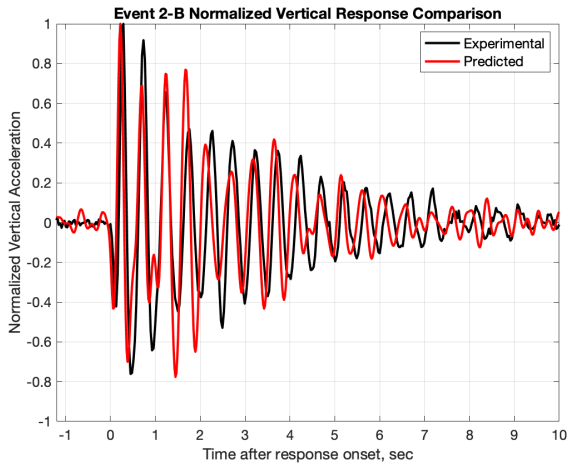

(a) Normalized Acceleration

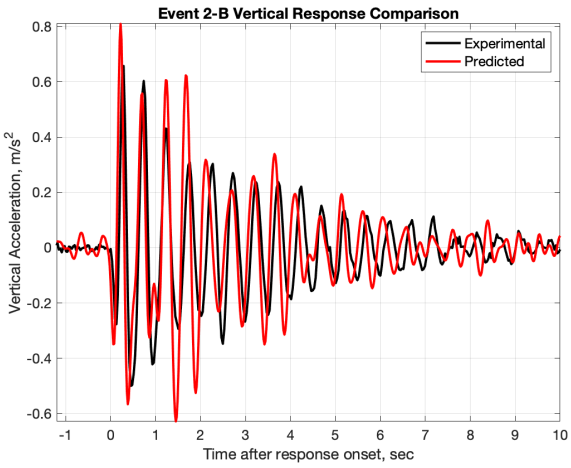

(b) Actual Acceleration

Figure 4-11. Comparison of experimental (black) and predicted (red) acceleration of the styrofoam box for Event 2-B. The amplitude in (a) is normalized by the maximum value, (b) the force on the ballon is $0.73F_b$.

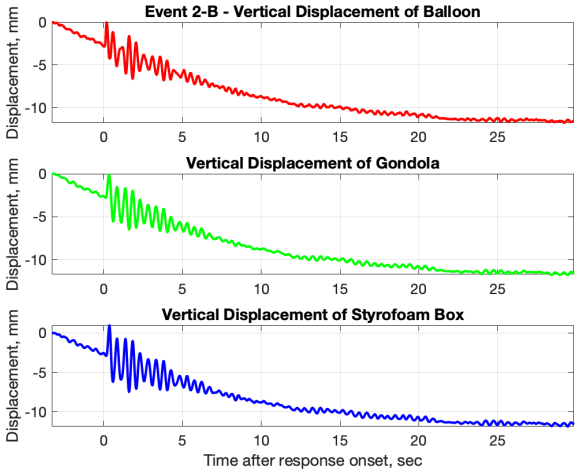

(a) Displacement

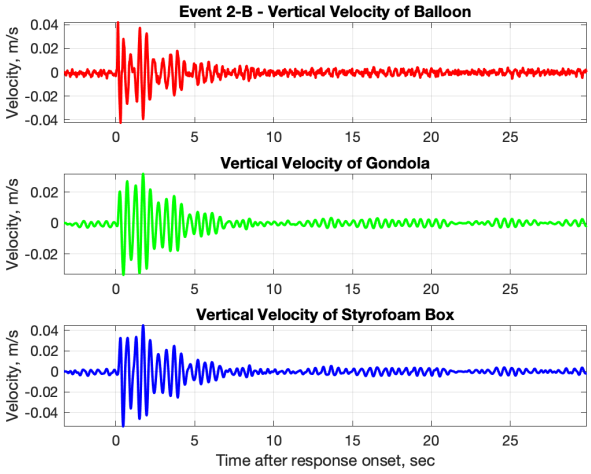

(b) Velocity

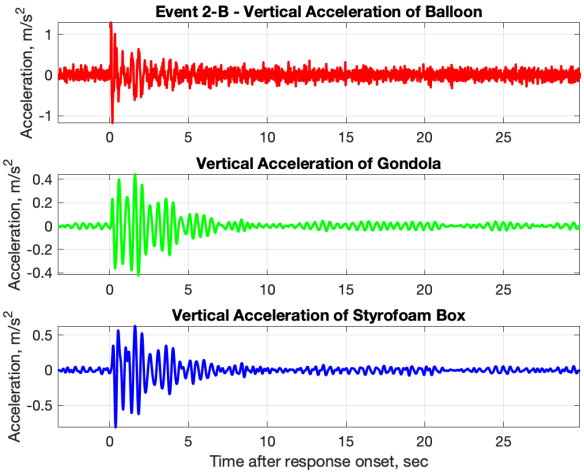

(c) Acceleration

Figure 4-12. Predicted response of the balloon, gondola and styrofoam box for Event 2-B: (a) displacement (in mm), (b) velocity and (c) acceleration.

5. CONCLUSIONS

The first steps have been completed in gaining an understanding of how balloon systems respond to incident infrasound signals. Starting from first principles, governing equations for the dynamic vertical motion of a balloon system have been developed. The dynamics was captured in a three degree of freedom lumped parameter model. By representing the balloon, gondola and styrofoam instrumentation box as rigid spheres, an analytical transfer function was developed relating the frequency dependent amplitude of the infrasound signal to the net force applied to the spheres. Further, this allowed the viscous damping associated with oscillatory motion and the added mass to be easily included, improving the physical accuracy of the model. The detrended experimental microbarometer data was convolved with the transfer function to give a prediction of the time-varying force on the balloon components. The predicted force on the balloon was scaled to account for the impedance mismatch between the helium in the envelope and the outside air. Expressing the governing equations as a system of first-order differential equations, the Runge-Kutta method was used to numerically time integrate the equations with the predicted forces. The numerical integration produced predictions of the vertical displacement, velocity and acceleration of each of the balloon components.

The predicted vertical acceleration of the styrofoam instrumentation box was compared to the measured accelerations for Events 1 and 2. Unknown damping coefficients for the balloon-gondola connection and the tether Paracord were estimated by comparing the normalized accelerations in the frequency domain. Excellent agreement was observed between the predicted and experimental accelerations. The dominant resonances of the balloon system aligned with the experimental data, indicating the stiffnesses were sufficiently accurate. The decay of the predicted acceleration followed the experimental trend giving support to the degree of damping in the model. A slight increase in the stiffness was needed for Event 2. It is postulated that solar radiation at the high altitude may have changed the material properties of the Paracord and strappings. With the updated stiffness, excellent agreement was observed with the measured acceleration for Event 2.

Overall the results suggest the vertical model of the balloon system captures the necessary physics. The agreement with the experimental data indicates the mass, stiffness and damping in the model is correct. The next step will be to implement the governing equations for a double pendulum to capture the swinging motion of the balloon system. The double pendulum formulation will predict the acceleration in the horizontal plane as well as the vertical. The horizontal accelerations are used in the direction of arrival and geolocation post-processing algorithms developed elsewhere for the experimental data. Once the full motion of the balloon system is understood, the governing equations will be used to guide improvements in the sensitivity and accuracy of the aeroseismometer system.

REFERENCES

[1] M. Abramowitz and I. A. Stegun. *Handbook of Mathematical Functions with Formulas, Graphs, and Mathematical Tables*. New York: Dover Publications, 1972.

[2] W. J. Anderson and I. Taback. Oscillation of high-altitude balloons. *Journal of Aircraft*, 28(9):606–608, 1991.

[3] H. F. Davis. *Fourier Series and Orthogonal Functions*. Dover Publications Inc., New York, 1963.

[4] R. W. Fox and A. T. McDonald. *Introduction to Fluid Mechanics*. John Wiley & Sons, Inc., New York, 4^{th} edition, 1992.

[5] L. D. Landau and E. M. Lifshitz. *Fluid Mechanics*. Pergamon Press, Oxford, 2^{nd} edition, 1987.

[6] MATLAB. *9.11.0.1769968 (R2021b)*. The MathWorks, Inc., 2021.

[7] L. M. Milne-Thomson. *Theoretical Hydrodynamics*. The Macmillan Company, New York, 1966.

[8] S. S. Rao. *Mechanical Vibrations*. Addison-Wesley Publishing Company, Inc., 3^{rd} edition, 1995.

DISTRIBUTION

Email—Internal

Name	Org.	Sandia Email Address
Danny Bowman	6752	dbowma@sandia.gov
Jerry Rouse	1553	jwrouse@sandia.gov
Elizabeth Silber	8911	esilbe@sandia.gov
Alex Sinclair	6752	amsincl@sandia.gov
Technical Library	1911	sanddocs@sandia.gov

Email—External

Name	Company Email Address	Company Name
Tai Lam	Tai.A.Lam@boeing.com	Boeing
Lt. Colonel Lewis	charlton.lewis@darpa.mil	DARPA

Sandia National Laboratories

Sandia National Laboratories is a multimission laboratory managed and operated by National Technology & Engineering Solutions of Sandia LLC, a wholly owned subsidiary of Honeywell International Inc., for the U.S. Department of Energy's National Nuclear Security Administration under contract DE-NA0003525.